

Cite this: *Catal. Sci. Technol.*, 2022,
12, 6556

New monoclinic ruthenium dioxide with highly selective hydrogenation activity†

Hee Jung Yang,^a Morgan Redington,^b Daniel P. Miller,^c Eva Zurek,^{*b} Minseob Kim,^d Choong-Shik Yoo,^d Soo Yeon Lim,^e Hyeonsik Cheong,^e Seen-Ae Chae,^f Docheon Ahn^g and Nam Hwi Hur^{*,a}

Catalytic hydrogenation of aromatic compounds is an important industrial process, particularly for the production of many petrochemical and pharmaceutical derivatives. This reaction is mainly catalyzed by noble metals, but rarely by metal oxides. Here, we report the development of monoclinic hydrogen-bearing ruthenium dioxide with a nominal composition of H_xRuO_2 that can serve as a standalone catalyst for various hydrogenation reactions. The hydrogen-bearing oxide was synthesized through the water gas shift reaction of CO and H_2O in the presence of rutile RuO_2 . The structure of H_xRuO_2 was determined by synchrotron X-ray diffraction and density functional theory (DFT) studies. Solid-state 1H NMR and Raman studies suggest that this compound possesses two types of isolated interstitial protons. H_xRuO_2 is very active in hydrogenation of various arenes, including liquid organic hydrogen carriers, which are completely converted to the corresponding fully hydrogenated products under relatively mild conditions. In addition, high selectivities (>99%) were observed for the catalytic hydrogenation of functionalized nitroarenes to corresponding anilines. DFT simulations yield a small barrier for concerted proton transfer. The facile proton dynamics may be key in enabling selective hydrogenation reactions at relatively low temperature. Our findings inspire the search for hydrogen-containing metal oxides that could be employed as high-performance materials for catalysts, electrocatalysts, and fuel cells.

Received 2nd May 2022,
Accepted 25th July 2022DOI: 10.1039/d2cy00815g
rsc.li/catalysis

Introduction

Heterogeneous catalytic hydrogenation is an important industrial process in which hydrogenation is carried out with molecular hydrogen (H_2) in the presence of a catalyst. Typical catalysts are based on noble metal nanoparticles (NPs) such as platinum (Pt),¹ palladium (Pd),² rhodium (Rh),³ and ruthenium (Ru),⁴ which are immobilized on a support with a large surface area. The supported NPs are active in a wide range of hydrogenation reactions under relatively mild conditions, but do not always ensure high selectivity for the

desired product. This reduced selectivity is mainly due to the high reactivity of noble metal NPs. To tune the reactivity of active metal NPs, individual atoms dispersed in reducible oxides have been investigated and found to be selective hydrogenation catalysts in many important reactions.^{5,6} Notably, it has been found that the active site of the hydrogenation reaction is not a pure metal, but an oxidized metal species. Somorjai and colleagues reported that oxygen strongly bound to the platinum surface affects the selectivity as well as the activity of a hydrogenation reaction.⁷ Catalytically active sites may thus be neither metals nor metal oxides, but may be in between.

Metal oxides generally act as supports or promoters for the active catalyst. In fact, metal oxides used as sole catalysts are rare, especially in hydrogenation reactions. Surprisingly, cerium oxide (CeO_2) turned out to be an efficient catalyst for gaseous hydrogenation from alkyne to olefin without the need for noble metals.⁸ Spectroscopic studies on well-ordered CeO_2 films in combination with density functional theory (DFT) calculations suggest that oxygen vacancies within CeO_2 play a crucial role in the incorporation of hydrogen (H) into the bulk and promote hydrogenation reactions.⁹ Numerous efforts have been made to investigate the interaction between hydrogen and metal oxides,^{10–12} but little is known about the

^a Department of Chemistry, Sogang University, Seoul 04107, Korea.
E-mail: nhhur@sogang.ac.kr

^b Department of Chemistry, State University of New York at Buffalo, Buffalo, NY 14260, USA. E-mail: ezurek@buffalo.edu

^c Department of Chemistry, Hofstra University, Hempstead, NY 11549, USA

^d Department of Chemistry, Institute for Shock Physics, Washington State University, Pullman, WA 99164, USA

^e Department of Physics, Sogang University, Seoul 04107, Korea

^f Western Seoul Center, Korea Basic Science Institute, Seoul 03759, Korea

^g Beamline Research Division, Pohang Accelerator Laboratory, Pohang University of Science and Technology, Pohang 37673, Korea

† Electronic supplementary information (ESI) available. See DOI: <https://doi.org/10.1039/d2cy00815g>



potential of hydrogen insertion to confer metal oxides with superior catalytic activity under ambient conditions. Thus, it is desirable to investigate H-bearing metal oxides as candidates for selective hydrogenation catalysts.

Here, we present the synthesis, characterization, and catalytic activity of a new H-bearing ruthenium dioxide denoted as H_xRuO_2 . Ru-based catalysts have been continuously studied because of the lower cost of Ru compared to Pd and Pt as well as the superior catalytic activity for a wide range of reactions. Moreover, they have been regarded as one of the most active catalysts for several industrially important reactions. The inclusion of hydrogen in reducible ruthenium oxide is exceptional and unprecedented. Unlike rutile RuO_2 , H_xRuO_2 acts as a standalone catalyst and exhibits excellent activity in the hydrogenation of various arenes and nitro-arenes. Moreover, the H_xRuO_2 catalyst is recyclable and maintains structural integrity in both alkaline and acidic media. This combination of superior activity and high stability can be beneficial for the use of H_xRuO_2 in a wide range of potential applications, especially in catalysis and energy-related fields.

Results and discussion

Synthesis and characterization of H_xRuO_2

Hydrogen insertion requires special reaction conditions because annealing metal oxides under a hydrogen atmosphere typically forms metals or oxygen-deficient oxides

rather than H-inserted oxides. Several specialized methods are known for the synthesis of H-inserted oxides, including high-pressure high-temperature techniques,¹³ hydrogen spillover,¹⁴ electrochemical hydrogenation,¹⁵ and acid treatment.¹⁶ However, these methods did not succeed in inserting hydrogen into ruthenium dioxide (RuO_2). We have developed a soft chemical approach based on the water gas shift reaction, which produces gaseous hydrogen at the expense of carbon monoxide ($CO + H_2O \rightleftharpoons CO_2 + H_2$).¹⁷ The reaction was performed at temperatures below 200 °C to prevent the formation of Ru NPs and to gently insert hydrogen into the host oxide lattice.

Fig. 1a shows powder X-ray diffraction (XRD) patterns of newly synthesized H_xRuO_2 , rutile RuO_2 , and hydrous $RuO_2 \cdot xH_2O$. The XRD spectrum of H_xRuO_2 shows several distinct peaks that do not match those of known materials, indicating that H_xRuO_2 adopts a new phase. A structural change might occur upon the insertion of hydrogen into the rutile RuO_2 matrix. The successful synthesis of H_xRuO_2 demonstrates the occurrence of hydrogen spillover on oxide surfaces, followed by chemical and structural transformations induced by coupled proton-electron transfer.¹⁸ Although the formation mechanism is currently not well understood, the insertion reaction appears to be facilitated by oxygen vacancies in ruthenium dioxide.¹⁹

The presence of hydrogen in H_xRuO_2 was confirmed by solid-state 1H NMR spectroscopy, which is a powerful technique capable of determining hydrogen species and their

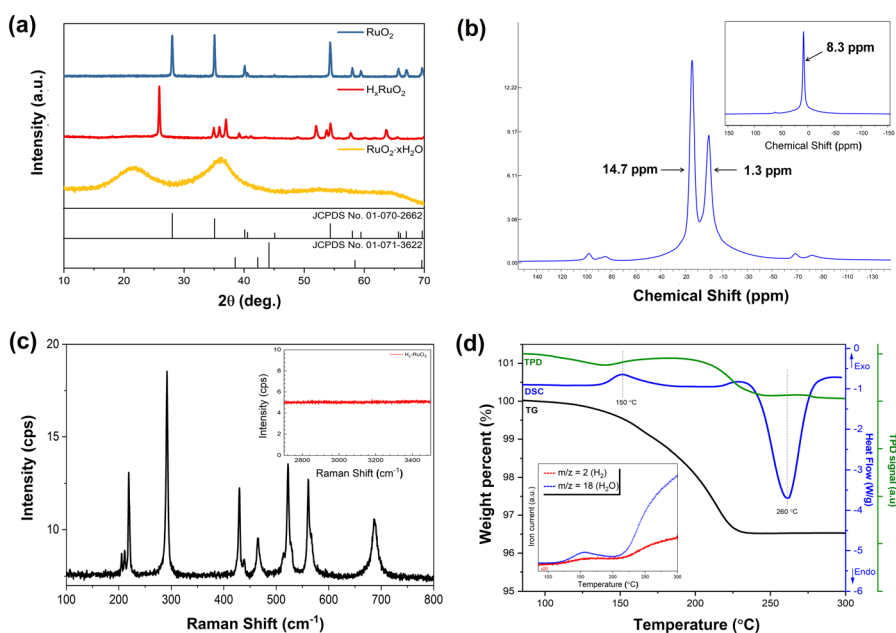


Fig. 1 Phase identification, spectroscopic characterization, and thermal analysis of H_xRuO_2 . (a) Powder XRD profiles of newly synthesized H_xRuO_2 , rutile RuO_2 , and hydrous $RuO_2 \cdot xH_2O$. Vertical lines on the bottom panel show the positions and intensities for RuO_2 and Ru taken from the JCPDS powder diffraction file. (b) Solid-state 1H MAS NMR spectrum for H_xRuO_2 showing two distinct peaks at 1.3 and 14.7 ppm. The inset is the 1H MAS NMR spectrum for $RuO_2 \cdot xH_2O$. (c) Raman spectra of H_xRuO_2 . The inset shows an expanded view of the Raman spectrum for H_xRuO_2 at higher frequencies. (d) Combined TGA (black line), DSC (blue line), TPD-MS (green line) curves for typical H_xRuO_2 sample as a function of temperature. The large mass change corresponds to the conversion of H_xRuO_2 to RuO_2 , which is accompanied by an endothermic signal in DSC and a water release in TPD-MS. The inset is MS signals of H_2O (blue line) and H_2 (red line) obtained from the TPD-MS measurement.



chemical environment in the oxide framework. Fig. 1b shows the magic angle spinning (MAS) ^1H NMR spectrum for $\text{H}_x\text{-RuO}_2$, illustrating two peaks at 1.3 and 14.7 ppm. For comparison, we measured the ^1H NMR spectrum for hydrous $\text{RuO}_2 \cdot x\text{H}_2\text{O}$ (see inset). The single broad peak at 8.3 ppm is attributed to water, suggesting that the two peaks in $\text{H}_x\text{-RuO}_2$ are not ascribed to protons in the structural water moiety. Based on the analysis of ^1H NMR involved in hydrogen bonding,²⁰ one peak at 14.7 ppm can be assigned to protons involved in the hydrogen bond, while the other signal at 1.3 ppm can be attributed to interstitial protons interacting weakly with neighboring oxygen and ruthenium atoms. The experimentally obtained chemical shifts are in good agreement with those computed *via* DFT for structure models with interstitial protons, as discussed in the ESI.†

Raman spectroscopy was used to obtain additional information about the crystal structure and chemical bonding of $\text{H}_x\text{-RuO}_2$, whose Raman spectrum (Fig. 1c) displays a new set of sharp peaks below 800 cm^{-1} , but no signals in the range of 800 to 4000 cm^{-1} . This indicates that neither signals attributed to the hydroxyl (O–H) group nor the water H–O–H moiety are observable in $\text{H}_x\text{-RuO}_2$.²¹ Below 800 cm^{-1} the calculated spectrum of the most stable structure identified *via* DFT calculations, a $P2_1/c$ symmetry RuO_2H phase, was in good agreement with experiment (Fig. S1†). However, at higher wavenumbers it possessed peaks associated with O–H wagging and stretching modes, not seen in experiment. As described below, first principles molecular dynamics (FPMD) calculations suggest that O–H \cdots O to O \cdots H–O proton exchange ought to be facile in this structure at room temperature. This can result in broadening of the O–H peaks, making them experimentally undetectable.

The chemical environments of Ru and O were evaluated by X-ray photoelectron spectroscopy (XPS). Particularly, the oxidation state of Ru and the bonding nature of O were examined through XPS analysis. The XPS spectra of $\text{H}_x\text{-RuO}_2$ are shown in Fig. S2† and were analyzed based on the published literature for common Ru materials.²² The fitting of the O 1s peak clearly indicates the presence of hydrogen that interacts with oxygen. The broad 3d peak structure, which can be fitted with several symmetric curves, suggests the presence of multiple oxidation states including Ru^{3+} and Ru^{4+} ions. The Ru metal peak, which usually appears around 280.0 eV , was not detected.

Thermal analysis

To obtain quantitative information on the hydrogen stoichiometry in $\text{H}_x\text{-RuO}_2$, thermogravimetric analysis (TGA) was conducted. Differential scanning calorimetry (DSC) and temperature programmed desorption-mass spectrometry (TPD-MS) measurements were also performed to evaluate the thermal stability of $\text{H}_x\text{-RuO}_2$. Fig. 1d shows typical TGA, DSC, and TPD-MS curves for $\text{H}_x\text{-RuO}_2$, collected in an inert gas atmosphere, as a function of temperature. The TGA curve shows a gradual weight loss up to about $230\text{ }^\circ\text{C}$ and no

further weight loss above $230\text{ }^\circ\text{C}$. The DSC curve exhibits a weak exothermic peak at $150\text{ }^\circ\text{C}$ and a distinct endothermic peak related to water loss at $260\text{ }^\circ\text{C}$. The exothermic peak appears to be associated with the structural transition from monoclinic to orthorhombic or tetragonal due presumably to hydrogen loss. The endothermic DSC signal at $260\text{ }^\circ\text{C}$ corresponds well with a significant weight loss observed in the TGA curve. Moreover, the temperature-dependent tendency of the TPD curve is very similar to those of the TGA and DSC curves.

As shown in the inset of Fig. 1d, H_2O ($m/z = 18$) evolution was clearly observed in the TPD-MS curve, which follows weight changes on the TGA curve. In addition to H_2O signals, H_2 ($m/z = 2$) gas evolution was detected. The H_2O mass spectrum shows a small peak at around $150\text{ }^\circ\text{C}$ and a large peak starting at around $230\text{ }^\circ\text{C}$, which also agrees with the TGA and DSC curves.

To determine the exact content of hydrogen in $\text{H}_x\text{-RuO}_2$, TGA measurements were performed in air using five different samples prepared under identical conditions (Fig. S3†). The average weight loss calculated from the TGA data was 6.61%. The overall composition can be established as $\text{H}_x\text{-RuO}_2$ ($x = 0.98$), which corresponds to nearly one equivalent of hydrogen per formula unit.

Structural characterization

The structure of $\text{H}_x\text{-RuO}_2$ was determined from Rietveld refinement of high-resolution synchrotron XRD data using the computationally predicted monoclinic $P2_1/c$ RuO_2H structure described in the ESI† as a starting model. First, we refined the positions of the Ru and O atoms and then two partially occupied H positions were included in the refined structure. A Fourier map constructed from the difference between the observed pattern and hydrogen-free refined structural model was employed to determine the positions of the hydrogen atoms.^{23,24} Two non-equivalent positions, H1 and H2, were found and their parameters were refined until a satisfactory fit was obtained. The occupation factors of the H1 and H2 sites were set to 0.49 each, based on the TGA data. This $P2_1/c$ model, including hydrogen positions, fit superbly to the synchrotron XRD data. Fig. 2a shows the Rietveld refinement of the synchrotron data to the model, which includes the observed, calculated, and difference diffraction patterns. The final refined structure is illustrated in Fig. 2b. As seen in Fig. 2c and d, the locations of the hydrogen atoms are imaged as dotted red circles that have high residual electron densities. The final crystallographic data and structural parameters are shown in Table S1.† Selected interatomic distances and angles are given in Table S2.†

Unlike the rutile structure with four long (2.026 \AA) and two short (1.869 \AA) Ru–O bonds,²⁵ $\text{H}_x\text{-RuO}_2$ has a distorted monoclinic structure with six different Ru–O bonds ranging from 1.993 to 2.148 \AA . Two short and long Ru \cdots Ru distances, 2.519 and 3.149 \AA , alternate along the c axis. A notable feature is the shortest Ru \cdots Ru separation (2.519 \AA), which is



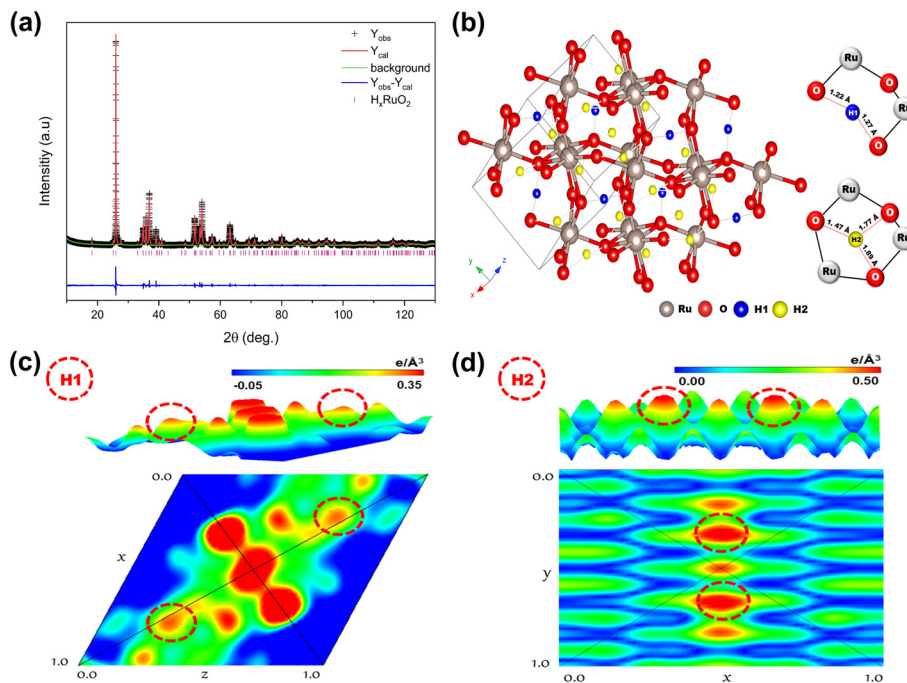


Fig. 2 Structural characterization of H_xRuO_2 . (a) Rietveld refinement profile of H_xRuO_2 . Observed (black crosses) and calculated (red solid line) synchrotron XRD intensities for H_xRuO_2 . Vertical bars show the Bragg peak positions. The difference plot is shown at the bottom. (b) The schematic structures for H_xRuO_2 . The structure is drawn so that the location of the H atoms can be easily seen. Gray and red spheres denote ruthenium and oxygen atoms, respectively. The Ru atoms occupy distorted RuO_6 octahedral sites. Hydrogen (H) atoms are represented by small spheres, where H1 and H2 are blue and yellow spheres, respectively. (c) The difference Fourier map of H_xRuO_2 in cross section with H1, showing the change in hydrogen distribution in H1. The dotted circles in maps (c and d) indicate the positions of H atoms. (d) The difference Fourier map of H_xRuO_2 in cross section with H2, showing the change in hydrogen distribution in H2.

comparable to the Ru–Ru bond length (2.650 Å) in hexagonal Ru metal, indicating the presence of metallic Ru–Ru bonds. The H1 proton interacts closely with two oxygen atoms at distances of 1.224 and 1.269 Å, while the H2 proton interacts weakly with three oxygen atoms at distances of 1.474 to 1.889 Å (Fig. 2b). These bonding properties are consistent with the aforementioned spectroscopic results.

Hydrogenation of arenes catalysed by H_xRuO_2

To test the catalytic activity of H_xRuO_2 , we began our investigation by evaluating the hydrogenation of toluene. Toluene was chosen as the model substrate because it is considered an efficient liquid organic hydrogen carrier (LOHC).²⁶ Catalytic hydrogenation was performed without solvent in an autoclave. For comparison, toluene

hydrogenation activity was also tested using rutile RuO_2 and commercial Ru catalyst. The commercial catalyst, 5 wt% of Ru loaded onto Al_2O_3 ($Ru@Al_2O_3$), is widely used as a catalyst for numerous hydrogenation reactions. The surface areas of rutile RuO_2 , H_xRuO_2 , and $Ru@Al_2O_3$ determined from the Brunauer–Emmett–Teller (BET) analysis, are 4.0, 27.8 and 118.9 $m^2 g^{-1}$, respectively (Fig. S4†). Typical SEM images of H_xRuO_2 (Fig. S5†) indicate micron-sized powders, which are consistent with the BET data.

The reaction results are summarized in Table 1. When using the H_xRuO_2 as a catalyst, complete conversion of toluene to methyl cyclohexane was achieved under 2 MPa of H_2 at 50 °C within 1 h (Table 1, entry 1). Methyl cyclohexane was observed as the sole product, and no partial hydrogenation products such as methyl cyclohexene and methyl cyclohexadiene were identified. Performing the same

Table 1 Hydrogenation of toluene to methylcyclohexane catalyzed by ruthenium-based catalysts

Entry ^a	Catalyst	Temperature [°C]	Pressure [MPa]	Time [h]	Conversion [%]
1	H_xRuO_2	50	2	1	>99
2	RuO_2	50	2	1	30.1
3	$Ru@Al_2O_3$ ^b	50	2	1	57.5
4	H_xRuO_2	25	4	2	>99
5	RuO_2	25	4	2	N.D.
6	$Ru@Al_2O_3$	25	4	2	15.3

^a Reaction condition: batch reactor, toluene (1 mL, 9.4 mmol), catalyst (10 mg). ^b 5 wt% ruthenium on alumina; N.D.: not detected.



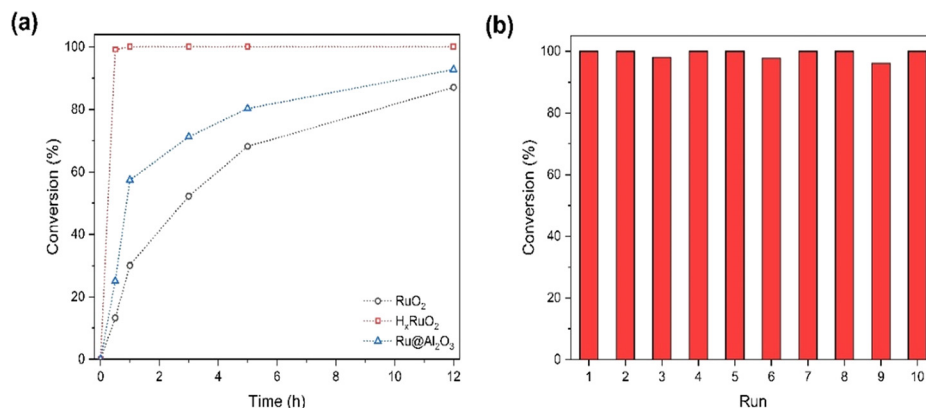


Fig. 3 Catalytic performance in the hydrogenation of toluene. (a) Comparison of the conversion over reaction time using three different catalysts. Reaction conditions: toluene (1 mL, 9.4 mmol), catalyst (10 mg), 2 MPa H₂, 50 °C. (b) Study on recyclability study of the H_xRuO₂ catalyst. Reaction conditions: toluene (1 mL, 9.4 mmol), catalyst (10 mg), 4 MPa H₂, room temperature, 2 h.

reaction in the presence of rutile RuO₂, however, the yield of methyl cyclohexane decreased to 30% (Table 1, entry 2). The Ru@Al₂O₃ catalyst exhibits only 57% conversion of toluene (Table 1, entry 3). Fig. 3a displays the conversion of toluene over the three catalysts as a function of time. We note that rapid hydrogen uptake occurs at the beginning of the reaction with the H_xRuO₂ catalyst, as shown in Fig. 3a. The conversions using the RuO₂ and Ru@Al₂O₃ catalysts increase with increasing reaction time, but full conversions were not reached even after 12 hours of reaction. This clearly suggests that H_xRuO₂ has a standalone catalytic function, especially for hydrogenation reactions.

The effect of H₂ pressure on toluene hydrogenation was also examined. When 4 MPa of H₂ was applied, toluene hydrogenation in the presence of H_xRuO₂ was completed even at room temperature within 2 h (Table 1, entry 4). In contrast, the RuO₂ catalyst did not show any activity and the Ru@Al₂O₃ catalyst gave considerably lower conversion (Table 1, entries 5 and 6). This indicates that pressure plays a key role in promoting the activity of H_xRuO₂, while the pressure had little effect on the RuO₂ and Ru@Al₂O₃ catalysts. The pressure-enhanced activity of H_xRuO₂ might be ascribed to interstitial protons in the RuO₂ lattice. The protic hydrogen seems to be highly mobile and strongly reactive under high H₂ pressure. Chen *et al.* reported a novel state of hydrogen with extremely high mobility in hydrogenated Nb₂O₅ and WO₃, which quickly reduces Cu²⁺ ions into Cu⁰ *via* proton transfer but has a very short lifetime.²⁷ On the other hand, protons in H_xRuO₂ are mobile and also exhibit a high stability, as evidenced by the intact XRD pattern of H_xRuO₂ after annealing at 150 °C at 2 MPa of H₂. Next, we studied the stability of the H_xRuO₂ catalyst because recycling used catalysts is an essential part of the economic evaluation of arene hydrogenation. Therefore, catalyst reuse experiments were conducted to prove the recyclability of H_xRuO₂. The catalytic activity of the used catalyst is shown in Fig. 3b. Complete conversion of toluene was evident even after ten cycles and any noticeable deactivation of the catalyst was not detected. In addition, no structural change was observed,

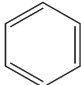
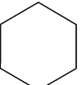
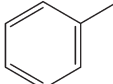
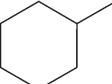
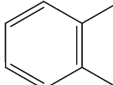
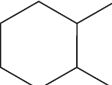
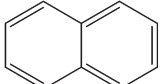
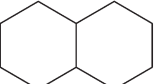
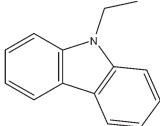
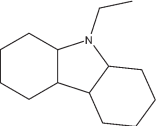
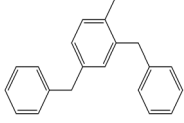
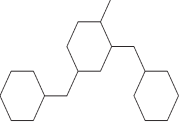
which was confirmed by powder XRD. The recycling results demonstrate that the H_xRuO₂ catalyst retains high activity against repeated toluene hydrogenations and can be used in industrially relevant continuous processes. In contrast, the catalytic activity of rutile RuO₂ decreased with increasing cycles under the same conditions, mainly because RuO₂ is easily decomposed into Ru. This indicates that the presence of hydrogen in H_xRuO₂ plays an important role in stabilizing the oxide framework.

The catalytic performance of Ru-based catalysts for converting toluene to methyl cyclohexane reported in the literature is summarized in Table S3† for comparison. The Ru catalysts supported on various materials exhibit superior activity in toluene hydrogenation, but temperatures higher than 100 °C are required for complete conversion (Table S3,† entries 1–6). Very recently, low temperature catalytic activity in aromatic hydrogenation has been identified using alkali-modified Ru–Na catalysts,²⁸ which was performed at 60 °C and 2 MPa of H₂ (Table S3,† entry 7). As seen in entry 8, H_xRuO₂ showed similar hydrogenation activity at lower temperatures and pressures than the Ru–Na catalyst. By simply raising the H₂ pressure to 4 MPa, moreover, the hydrogenation of toluene is completed within 2 h even at 25 °C. (Table S3,† entry 9). Compared to previously known heterogeneous Ru-based catalysts, the H_xRuO₂ catalyst shows better catalytic performance for toluene hydrogenation. It is worth mentioning that catalysts operating at low temperatures are important because hydrogenation is an exothermic reaction that can break C–C bonds.

To expand the scope of arene hydrogenation using the H_xRuO₂ catalyst, we investigated the reactivity of various arene substrates in the absence of solvent. Table 2 shows the best results optimized for complete conversion of arenes into corresponding fully hydrogenated products. Like toluene hydrogenation, the conversion of benzene to cyclohexane proceeded smoothly at room temperature (Table 2, entry 1). However, for xylene, a full conversion was achieved at 60 °C (Table 2, entry 3). Benzene, toluene, and xylene, which are referred to as BTX in the petrochemical industry, were readily converted to the corresponding saturated hydrocarbons



Table 2 Hydrogenation of various arenes catalyzed by H_xRuO₂

Entry ^a	Substrate	Product	Temperature [°C]	Pressure [MPa]	Time [h]	Conversion [%]	Selectivity [%]
1			25	4	0.8	>99	>99
2			25	4	1	>99	>99
3			25	4	2	>99	>99
4 ^b			120	5	3	>99	>99
5 ^c			120	5	3	>99	>98 ^d
6 ^c			120	5	3	>99	>99 ^e

^a Reaction condition: batch reaction, substrate (9.4 mmol), catalyst (20 mg), reaction mixture stirred at 600 r.p.m. ^b Substrate (5 mmol). ^c Substrate (1 mmol). ^d Selectivity to H12-NEC. ^e Selectivity to H18-DBT.

under mild conditions. Naphthalene, which is the simplest polycyclic aromatic hydrocarbon and is a crystalline solid, was converted to the fully hydrogenated product, decalin. Remarkably, decalin is formed as the sole product through a solid-state reaction (Table 2, entry 4).

N-Ethylcarbazole (H0-NEC) and dibenzyltoluene (H0-DBT) are also regarded as promising future LOHC materials.^{29,30} The H_xRuO₂ catalyst was investigated for the hydrogenation of the two LOHCs. *N*-ethyl-dodecahydro-carbazole (H12-NEC) along with partially hydrogenated products were obtained under 4 MPa of H₂ at 120 °C. However, increasing the pressure of H₂ to 5 MPa completely converts H0-NEC to H12-NEC within 3 h. Next, the hydrogenation of dibenzyltoluene (H0-DBT) was evaluated under similar reaction conditions. Complete conversion of H0-DBT to perhydro dibenzyltoluene (H18-DBT) was achieved at 120 °C and 5 MPa for 3 h. When the hydrogenation reactions of H0-NEC and H0-DBT were performed in the presence of the Ru@Al₂O₃ catalyst, however, the yield of the desired products drastically decreased under identical conditions. Most of the hydrogenation reactions with Ru-based catalysts reported thus far have been investigated at temperatures higher than 150 °C to obtain higher yields ranging from 90 to 99%.

All these results show that H_xRuO₂ is catalytically more active, especially for hydrogenation reactions of aromatic compounds than rutile RuO₂ and commercial Ru@Al₂O₃ catalysts. Moreover, the catalytic reactions proceeded smoothly

in the absence of solvent and the H_xRuO₂ is quite stable even under harsh reducing conditions. The solventless hydrogenation of various arenes using the H_xRuO₂ catalyst might be attractive for industrial applications because neither solvent nor purification steps are required. In addition, the lack of additional steps reduces energy consumption and lowers capital investment. Therefore, it can be considered a more environmentally benign and cost-effective process.

Chemoselective hydrogenation of nitroarenes to anilines

To determine whether H_xRuO₂ could act as a chemoselective catalyst, we tested various nitroarenes that contained at least nitro and phenyl groups. They are challenging substrates because they have reducible moieties in addition to the nitro group. The resulting aniline and its derivatives are industrially important chemicals that are widely used as precursors for the manufacture of polymers, agrochemicals, and pharmaceuticals.^{31,32} Noble metal catalysts are well known for the reduction of nitroarenes to anilines. Because of their high reactivity, they often lead to the formation of undesirable by-products such as hydroxylamine.³³ The desired selectivity might be achieved by an oxide-based H_xRuO₂ catalyst.

Nitrobenzene was chosen as an initial model substrate to determine the optimal conditions for the hydrogenation reaction. The reaction was completed in a water-methanol solvent within 1 h at 60 °C under 0.5 MPa of H₂. The H_xRuO₂



Table 3 Hydrogenation of nitroarenes to anilines catalyzed by ruthenium-based catalysts

Entry ^a	Catalyst	Substrate	Temperature [°C]	Pressure [MPa]	Time [h]	Conversion [%]
1	H _x RuO ₂	Nitrobenzene	60	0.5	1.0	>99
2	RuO ₂	Nitrobenzene	60	0.5	1.5	29.1
3	Ru@Al ₂ O ₃ ^b	Nitrobenzene	60	0.5	1.5	27.0
4	H _x RuO ₂	<i>p</i> -Nitrophenol	40	0.5	1.0	>99
5	RuO ₂	<i>p</i> -Nitrophenol	40	0.5	1.0	9.5
6	Ru@Al ₂ O ₃ ^b	<i>p</i> -Nitrophenol	40	0.5	1.0	9.1

^a Reaction condition: batch reactor, stirring bar, substrate (1 mmol), solvent = methanol/H₂O (1 : 1) 2 mL, catalyst (10 mg). ^b 5 wt% ruthenium on alumina.

catalyst produces the desired aniline in excellent yield (>99%) with no by-products (Table 3, entry 1), clearly showing that H_xRuO₂ is an active catalyst for the chemoselective reduction of the nitro group. On the other hand, when RuO₂ and Ru@Al₂O₃ were used as catalysts under the same conditions, the yields dropped to less than 30% (Table 3, entries 2 and 3). Based on the optimized reaction conditions, 4-nitrophenol, which possesses a hydroxyl group *para* to the nitro group on the phenyl ring, was tested. The use of H_xRuO₂ produced the

desired 4-aminophenol in a yield greater than 99% (Table 3, entry 4), whereas much lower yields were obtained with RuO₂ and Ru@Al₂O₃ (Table 3, entries 5 and 6).

Next, the general scope of our H_xRuO₂ catalyst was demonstrated in the reduction of functionalized nitroarenes. As shown in Table S4,† they afforded the corresponding anilines in excellent yields over 99%. A notable finding is that substrates having slightly bulky electron-donating groups (Table S4,† entries 3 and 4) as well as nitroarenes containing

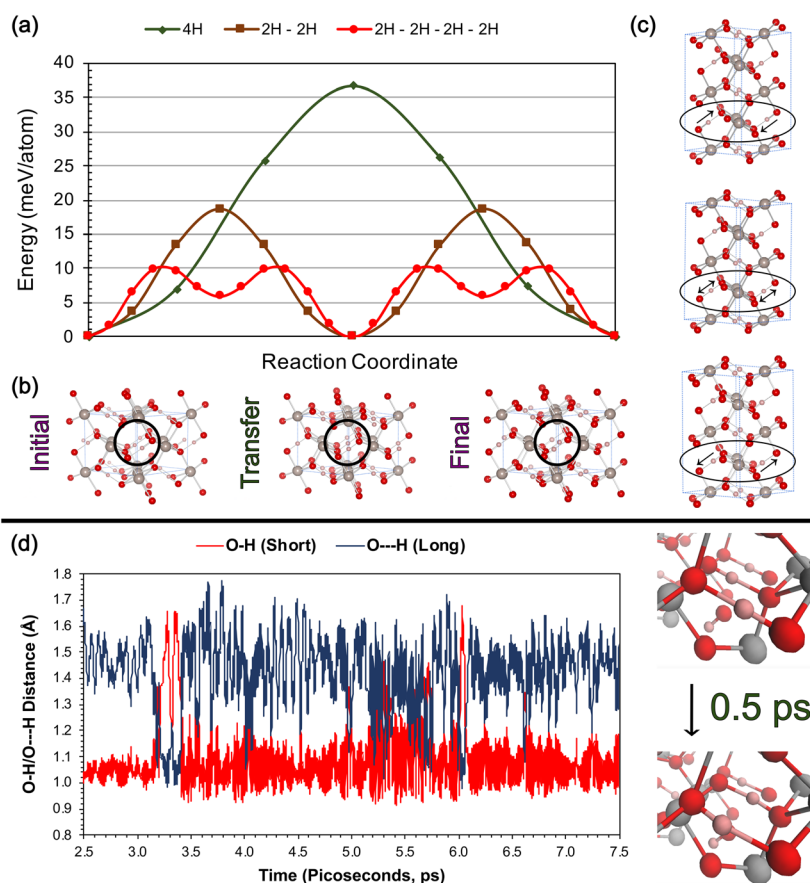


Fig. 4 Computational investigation of proton transfer energetics. (a) Comparison of simultaneous proton transfer (4H), concerted proton transfer (2H-2H), and concerted proton transfer in a $1 \times 2 \times 1$ supercell (2H-2H-2H-2H) energies determined via Nudged Elastic Band (NEB) calculations. (b) Initial, midpoint, and final proton transfer structures for simultaneous proton transfer (4H). (c) Initial, midpoint, and final proton transfer structures for concerted proton transfer in a $1 \times 2 \times 1$ supercell (2H-2H-2H-2H) with an emphasis placed on direction of proton motion. (d) O-H and O...H distances for a selected O-H...O bond during a FPMD simulation post-equilibration at 298 K in a $2 \times 2 \times 2$ supercell, showing multiple proton transfers during the simulation. Inset highlights a proton that undergoes an O...H-O to O-H...O transfer after about 0.5 ps of the simulation.



electron-withdrawing elements (Table S4,† entries 5 and 6) were smoothly hydrogenated under mild conditions. All these results clearly show that H_xRuO_2 not only outperforms rutile RuO_2 and commercial $Ru@Al_2O_3$ catalyst, but also acts as a catalyst for highly selective hydrogenations.

Catalytic significance of interstitial hydrogen in H_xRuO_2

To determine whether the interstitial protons are key for the catalytic activity, we investigated the hydrogenation of benzene using deuterated D_xRuO_2 . Catalytic hydrogenation of benzene was performed under the same conditions. Deuterated cyclohexane derivatives were identified from the reaction products by gas chromatography-mass spectrometer and 1H NMR, clearly showing a direct transfer of deuterium from D_xRuO_2 to benzene. The deuterium vacancies in D_xRuO_2 are replenished by dissociated H species. This suggests that interstitial protons within H_xRuO_2 play a crucial role in accelerating hydrogenation reaction.

Werner and coworkers reported spectroscopic evidence for the coexistence of surface and bulk H species upon H_2 dissociation over CeO_2 , suggesting that the Ce–H species are reactive enough to participate in the hydrogenation reaction.³⁴ Like the H_2 – CeO_2 interaction, the dissociation of H_2 occurs on H_xRuO_2 , producing dissociated H species. The H species diffuse over oxide surfaces and can easily jump from one site to another, which appears to be assisted by the presence of mobile protons in bulk H_xRuO_2 . This proton-hopping process might be related to the Grotthuss mechanism.³⁵ The vacant interstitial sites appear to serve as highly efficient conduits for rapid proton-hopping leading to the exceptional catalytic activity of H_xRuO_2 .

Computational studies

To better understand the barriers involved in the proton transfer density functional theory (DFT) nudged elastic band (NEB) calculations³⁶ were carried out on the $P2_1/c$ RuO_2H phase (Fig. 4a). When all four of the hydrogen atoms within a single unit cell (4H) were transferred simultaneously a barrier of ~ 37 meV per atom was obtained, with the initial, midpoint and final structures illustrated in Fig. 4b. A second stepwise 2H–2H mechanism was found wherein two hydrogens were initially transferred from O–H \cdots O into O \cdots H–O moieties, followed by an additional transfer of two hydrogens. This mechanism resulted in two barriers of 19 meV per atom each. Finally, a 2H–2H–2H–2H transfer mechanism in an RuO_2H supercell was found to possess an even smaller barrier, with intermediates that lay 6 meV per atom higher in energy than the ground state (Fig. 4c). The hydrogen atoms in the intermediates were found to lie slightly off center from the midpoint. Such a lowering of the barrier upon enlarging the cell used to model the structure suggests that the barrier would decrease further using larger supercells.

Further first-principles molecular dynamics (FPMD) simulations on a supercell of $P2_1/c$ RuO_2H showed that

hydrogen transfers occur spontaneously at room temperature. Selected O–H bond distances were plotted as a function of time (Fig. 4d) to analyze the proton dynamics. In a proton transfer event an O–H distance lengthened to 1.4–1.6 Å while at the same time an H \cdots O distance shortened to ~ 1.1 Å. Some protons that were transferred near the beginning of the FPMD run remained so during the full duration of the simulation, while others quickly returned to their respective short O–H bond lengths. The protons spent about 2.5% of the simulation time bonded to an oxygen atom that differed from the one in the starting geometry. Inclusion of anharmonic and quantum nuclear effects are likely to further enhance the degree of proton transfer. These computational studies suggest that the facile proton dynamics may be related to the remarkable catalytic activity of H_xRuO_2 .

Conclusions

In conclusion, we have developed a new ruthenium dioxide H_xRuO_2 that adopts a monoclinic structure with interstitial protons. H_xRuO_2 acts as a standalone catalyst, exhibits highly selective hydrogenation under mild conditions, and outperforms rutile RuO_2 and commercial $Ru@Al_2O_3$ catalysts. Furthermore, H_xRuO_2 is recyclable and stable in both acidic and alkaline media. The mobile proton embedded in the oxide lattice plays an important role in stabilizing the distorted structure and maintains the hydrogen flux without diffusion limitation, substantially enhancing the catalytic properties through coupled proton–electron transfer. The discovery of H_xRuO_2 and its excellent catalytic activity opens up new perspectives to explore H-bearing metal oxides that can serve as new exotic materials as well as hydrogenation catalysts.

Experimental methods

Synthesis of hydrogen-bearing ruthenium dioxide (H_xRuO_2)

In a 10 mL reaction vial, 0.30 g of polycrystalline RuO_2 was mixed with 0.3 mL of deionized water. The reaction vial was placed into a 45 mL autoclave. The autoclave was purged twice with CO and then pressurized to 1.5 MPa CO at room temperature. The autoclave was heated to 200 °C and maintained for 6 hours at 200 °C. After completion of the reaction, the autoclave was cooled to room temperature. The resulting black solid was washed with toluene three times and dried under vacuum for 2 hours. The typical yield of H_xRuO_2 based on the used RuO_2 was about 94% (0.28 g).

General procedure for catalytic hydrogenation

The catalytic hydrogenation was conducted in a 45 mL stainless autoclave. Typically, substrate was mixed with the H_xRuO_2 catalyst (10 mg) in a 10 mL reaction vial equipped with a magnetic stirring bar. The reaction vial was placed into the autoclave. The autoclave was purged twice with H_2 at room temperature, which was then pressurized with H_2 to 0.5–8.0 MPa. The autoclave was maintained at 25–120 °C with



stirring for a given period of time. After completion of the reaction, the autoclave was cooled to room temperature. The products were analyzed by NMR. NMR data of the products are given in the ESI.†

Computational details

Precise geometry optimizations, ¹H NMR chemical shifts, electronic density of states, band structure, first principles molecular dynamics (FPMD), and nudged elastic band (NEB) calculations were performed using density functional theory (DFT) with the Perdew–Burke–Ernzerhof (PBE) functional³⁷ as implemented in the Vienna *ab initio* simulation package (VASP).^{38,39} A plane wave basis set with an energy cutoff of 600 eV was used along with projector-augmented wave (PAW) potentials⁴⁰ where the H 1s¹, O 2s²2p⁴, and Ru 4d⁷5s¹ electrons were treated explicitly. Evolutionary structure searches were performed with the XTALOPT⁴¹ algorithm. Further computational details are provided in the ESI.†

Author contributions

H. J. Y. carried out the experiment and performed the characterization. M. R. and D. P. M. conducted the theoretical DFT simulations under the guidance of E. Z., M. K. and C. S. Y. contributed to the structure and Raman analysis. S. Y. L. conducted the Raman experiment under the guidance of H. C. and S. A. C. performed the solid state NMR spectroscopy. D. A. carried out the experiment at the beamline. N. H. H. conceived the project and directed the experiments. N. H. H. wrote the manuscript with contributions from all co-authors. All authors contributed to the discussion of the results.

Conflicts of interest

There are no conflicts to declare.

Acknowledgements

The work at SU (N. H. H.) was supported by the NRF funded by the Korean Government (MSIT) (grant no. NRF-2019R1A2C1003666 and 2021-JDH-2-SB1-1), the “Human Resources Program in Energy Technology” of the KETEP funded by the Korean Government (MOTIE) (grant no. 20194010201910). The authors (M. K. and C. S. Y.) at WSU acknowledge funding from the NSF (DMR 1701360 and 2112653) and DOE-NNSA (DE-NA0003918). E. Z. acknowledges the National Science Foundation (DMR-1827815) for financial support. Support was also provided by the Center for Computational Research at the University at Buffalo (<https://hdl.handle.net/10477/79221>). D. P. M. thanks both Hofstra University (start-up/FRDG) and the US National Science Foundation (CHE-2108597) for funding. The work at SU (H. C.) was supported by the NRF funded by the Korean Government (MSIT) (grant no. NRF-2019R1A2C3006189). The work at PLS-II were supported in part by MSIP and POSTECH.

The author (S. A. C.) acknowledge funding from the Ministry of Science and ICT in Korea *via* KBSI (Grant No. C123000).

References

- X. J. Jin, R. Tsukimura, T. Aihara, H. Miura, T. Shishido and K. Nozaki, *Nat. Catal.*, 2021, **4**, 312–321.
- G. Kyriakou, M. B. Boucher, A. D. Jewell, E. A. Lewis, T. J. Lawton, A. E. Baber, H. L. Tierney, M. Flytzani-Stephanopoulos and E. C. H. Sykes, *Science*, 2012, **335**, 1209–1212.
- D. Moock, M. P. Wiesenfeldt, M. Freitag, S. Muratsugu, S. Ikemoto, R. Knitsch, J. Schneidewind, W. Baumann, A. H. Schafer, A. Timmer, M. Tada, M. R. Hansen and F. Glorius, *ACS Catal.*, 2020, **10**, 6309–6317.
- X. J. Cui, A. E. Surkus, K. Junge, C. Topf, J. Radnik, C. Kreyenschulte and M. Beller, *Nat. Commun.*, 2016, **7**, 11326–11334.
- M. P. Wiesenfeldt, Z. Nairoukh, T. Dalton and F. Glorius, *Angew. Chem., Int. Ed.*, 2019, **58**, 10460–10476.
- A. Corma and P. Serna, *Science*, 2006, **313**, 332–334.
- C. E. Smith, J. P. Biberian and G. A. Somorjai, *J. Catal.*, 1979, **57**, 426–443.
- G. Vile, B. Bridier, J. Wichert and J. Perez-Ramirez, *Angew. Chem., Int. Ed.*, 2012, **51**, 8620–8623.
- Z. Wu, Y. Cheng, F. Tao, L. Daemen, G. S. Foo, L. Nguyen, X. Zhang, A. Beste and A. J. Ramirez-Cuesta, *J. Am. Chem. Soc.*, 2017, **139**, 9721–9727.
- Y. Filinchuk, N. A. Tumanov, V. Ban, H. Ji, J. Wei, M. W. Swift, A. H. Nevidomskyy and D. Natelson, *J. Am. Chem. Soc.*, 2014, **136**, 8100–8109.
- H. Cheng, M. Wen, X. Ma, Y. Kuwahara, K. Mori, Y. Dai, B. Huang and H. Yamashita, *J. Am. Chem. Soc.*, 2016, **138**, 9316–9324.
- I. S. Chopra, S. Chaudhuri, J. F. Veyan and Y. J. Chabal, *Nat. Mater.*, 2011, **10**, 884–889.
- A. J. Hupfer, E. V. Monakhov, B. G. Svensson, I. Chaplygin and E. V. Lavrov, *Sci. Rep.*, 2017, **7**, 17065.
- W. Karim, C. Spreafico, A. Kleibert, J. Gobrecht, J. VandeVondele, Y. Ekinci and J. A. van Bokhoven, *Nature*, 2017, **541**, 68–71.
- A. Sood, A. D. Poletayev, D. A. Cogswell, P. M. Csernica, J. T. Mefford, D. Fraggedakis, M. F. Toney, A. M. Lindenberg, M. Z. Bazant and W. C. Chueh, *Nat. Rev. Mater.*, 2021, **6**, 847–867.
- L. Xie, Q. Zhu, G. Zhang, K. Ye, C. Zou, O. V. Prezhdo, Z. Wang, Y. Luo and J. Jiang, *J. Am. Chem. Soc.*, 2020, **142**, 4136–4140.
- A. A. Gokhale, J. A. Dumesic and M. Mavrikakis, *J. Am. Chem. Soc.*, 2008, **130**, 1402–1414.
- L. R. Merte, G. W. Peng, R. Bechstein, F. Rieboldt, C. A. Farberow, L. C. Grabow, W. Kudernatsch, S. Wendt, E. Laegsgaard, M. Mavrikakis and F. Besenbacher, *Science*, 2012, **336**, 889–893.
- Y. D. Kim, A. P. Seitsonen, S. Wendt, J. Wang, C. Fan, K. Jacobi, H. Over and G. Ertl, *J. Phys. Chem. B*, 2001, **105**, 3752–3758.



- 20 K. Sutter, G. A. Aucar and J. Autschbach, *Chem. – Eur. J.*, 2015, **21**, 18138–18155.
- 21 H. C. Jo, K. M. Kim, H. Cheong, S. H. Lee and S. K. Deb, *Electrochem. Solid-State Lett.*, 2005, **8**, E39–E41.
- 22 D. J. Morgan, *Surf. Interface Anal.*, 2015, **47**, 1072–1079.
- 23 R. I. Cooper, A. L. Thompson and D. J. Watkin, *J. Appl. Crystallogr.*, 2010, **43**, 1100–1107.
- 24 A. Sano-Furukawa, T. Hattori, K. Komatsu, H. Kagi, T. Nagai, J. J. Molaison, A. M. dos Santos and C. A. Tulk, *Sci. Rep.*, 2018, **8**, 15520.
- 25 H. Over, *Chem. Rev.*, 2012, **112**, 3356–3426.
- 26 D. Teichmann, W. Arlt, P. Wasserscheid and R. Freymann, *Energy Environ. Sci.*, 2011, **4**, 2767–2773.
- 27 W. P. Chen, K. F. He, Y. Wang, H. L. L. W. Chan and Z. J. Yan, *Sci. Rep.*, 2013, **3**, 3149.
- 28 Q. Pei, T. He, Y. Yu, Z. J. Jing, J. P. Guo, L. Liu, Z. T. Xiong and P. Chen, *ACS Appl. Mater. Interfaces*, 2020, **12**, 7071–7080.
- 29 M. Niermann, S. Drunert, M. Kaltschmitt and K. Bonhoff, *Energy Environ. Sci.*, 2019, **12**, 290–307.
- 30 H. Jorschick, A. Bulgarin, L. Alletsee, P. Preuster, A. Bosmann and P. Wasserscheid, *ACS Sustainable Chem. Eng.*, 2019, **7**, 4186–4194.
- 31 R. V. Jagadeesh, A. E. Surkus, H. Junge, M. M. Pohl, J. Radnik, J. Rabeah, H. M. Huan, V. Schunemann, A. Bruckner and M. Beller, *Science*, 2013, **342**, 1073–1076.
- 32 M. Macino, A. J. Barnes, S. M. Althahban, R. Qu, E. K. Gibson, D. J. Morgan, S. J. Freakley, N. Dimitratos, C. J. Kiely, X. Gao, A. M. Beale, D. Bethell, Q. He, M. Sankar and G. J. Hutchings, *Nat. Catal.*, 2019, **2**, 873–881.
- 33 Q. Zhang, J. Bu, J. Wang, C. Sun, D. Zhao, G. Sheng, X. Xie, M. Sun and L. Yu, *ACS Catal.*, 2020, **10**, 10350–10363.
- 34 K. Werner, X. F. Weng, F. Calaza, M. Sterrer, T. Kropp, J. Paier, J. Sauer, M. Wilde, K. Fukutani, S. Shaikhutdinov and H. J. Freund, *J. Am. Chem. Soc.*, 2017, **139**, 17608–17616.
- 35 S. F. Parker, S. J. Robertson and S. Imberti, *Mol. Phys.*, 2019, **117**, 3417–3423.
- 36 G. Henkelman, B. P. Uberuaga and H. Jonsson, *J. Chem. Phys.*, 2000, **113**, 9901–9904.
- 37 J. P. Perdew, K. Burke and M. Ernzerhof, *Phys. Rev. Lett.*, 1996, **77**, 3865–3868.
- 38 G. Kresse and J. Furthmuller, *Phys. Rev. B: Condens. Matter Mater. Phys.*, 1996, **54**, 11169–11186.
- 39 G. Kresse and D. Joubert, *Phys. Rev. B: Condens. Matter Mater. Phys.*, 1999, **59**, 1758–1775.
- 40 P. E. Blochl, *Phys. Rev. B: Condens. Matter Mater. Phys.*, 1994, **50**, 17953–17979.
- 41 Z. Falls, P. Avery, X. Y. Wang, K. P. Hilleke and E. Zurek, *J. Phys. Chem. C*, 2021, **125**, 1601–1620.

